

# Superior Frequency Stability and Long-Lived State-Swapping in Cubic-SiC Mechanical Mode Pairs

Huanying Sun <sup>1,\*</sup>, Yanlin Chen,<sup>1,2,3,\*</sup> Qichun Liu,<sup>1,\*</sup> Haihua Wu,<sup>1</sup> Yuqing Wang,<sup>1</sup> Tiefu Li,<sup>4,1,†</sup> and Yulong Liu <sup>1,2,3,‡</sup>

<sup>1</sup>Beijing Key Laboratory of Fault-Tolerant Quantum Computing,  
Beijing Academy of Quantum Information Sciences, Beijing 100193, China

<sup>2</sup>Beijing National Laboratory for Condensed Matter Physics,  
Institute of Physics, Chinese Academy of Sciences, Beijing 100190, China

<sup>3</sup>University of Chinese Academy of Sciences, Beijing 100049, China

<sup>4</sup>School of Integrated Circuits and Frontier Science Center for Quantum Information, Tsinghua University, Beijing 100084, China

(Dated: July 9, 2025)

The multimode cavity optomechanical system offers versatile applications including state transduction, coherent interconnection, and many-body simulations. In this study, we developed a cavity electromechanical system that integrates a 3C-SiC membrane and a rectangular superconducting cavity to observe the generation of nearly degenerate pairs of mechanical modes. Subsequently, we derive the expression for intrinsic frequency under nonuniform stress and find that this method supports a remarkably resolution for stress analysis in thin films. Experimentally, we perform collective fitting on the measured set of 57 mechanical modes, revealing deviations in biaxial non-uniform stress on the order of MPa. These degeneracy-broken mechanical modes exhibit exceptional quality factors as high as  $10^8$  in a thermal bath of 10 mK. Furthermore, Allan deviation indicates that these modes exhibit extremely stable frequencies compared with different types of optomechanical devices. We then performed state-swapping between near-degenerate mode pairs, demonstrating the transfer efficiency exceeding 78%, attributed to their exceptionally long lifetimes. This study paves the way for the design of compact quantum phononic devices featuring high-quality-factor mechanical multimodes.

## Introduction

Phonons have broad applications in thermal management, materials science, and quantum information processing due to their ability to mediate interactions among heat, electricity, and light [1–3]. Multiple mechanical mode-based optomechanical and electromechanical systems not only hold promising applications in quantum memory [4–7] or quantum transduction [8–13], but also serve as ideal platforms for studying intriguing physical phenomenon, e.g., quantum entanglements [14–18], multimode phonon lasing [19–21], and nonreciprocal photon (phonon) transport [22–28]. Currently, multimode optomechanical or electromechanical systems are typically developed through two pathways: integrating electronic or optical cavities with spatially separated mechanical resonators [29–32], or utilizing different-order modes within a single mechanical resonator to couple with one cavity [33–36]. In the latter configuration, mechanical resonators of various geometries have attracted significant attention, including one-dimensional (1D) structures such as nanowires [37, 38] and cantilevers [39, 40], as well as phononic crystal beams [41–45]. Two-dimensional (2D) structures include membrane [29, 46, 47] and phononic bandgap shield resonators [48–52]. Three-dimensional (3D) structures encompass micro toroidal [39], disk [53–56], trapped-particles [57, 58], and surface or bulk acoustic mode-based devices [59–65]. Among these configurations, 2D structures such as sili-

con nitride (SiN) square membranes have been widely used in microwave electromechanical and cavity optomechanical systems due to their advantages of high-stress-induced dissipation dilution and high  $Q$  factors [66–70].

For a typical square-shaped membrane resonator under isotropic stress, the resonance frequencies of out-of-plane mode can be expressed as  $f_{mn} = \sqrt{(m^2 + n^2)\sigma/(4\rho L^2)}$ , where the  $m$  and  $n$  represent the node number of the mode shape,  $\sigma$  is the isotropic stress in the membrane, the  $\rho$  is the mass density, and  $L$  is the side length of the square [71]. In this scenario, modes become degenerate when they share the same mode indices  $m$  and  $n$ , hence resulting in the optomechanical coupling occurs only between a limited number of mechanical modes and cavity fields. For example, in microwave optomechanical devices integrated with SiN films, the coupling electrodes typically interact with only one mode of the degenerate mode pair within the microwave cavity [72–74]. In addition, the dark modes that spontaneously form from degenerate mechanical modes will hinder ground state cooling [75, 76], and the preparation of macroscopic squeezed or entangled states [77–80].

It is worth noting that the introduction of asymmetric stress along the x-axis and y-axis in the membrane would break the degenerate mechanical resonance state with equal node numbers [81, 82]. The altered states may exhibit similar vibration mode shapes with rotational symmetry, potentially leading to a similar coupling strength between the optical mode and all modified mechanical modes [83–87]. Although the degeneracy breaking of mechanical modes in square membrane resonators has been observed in some studies, however, measur-

\* These authors contributed equally to this work.

† litf@tsinghua.edu.cn

‡ liuyul@baqis.ac.cn

ing the asymmetry of stress in thin films with high precision is challenging for the traditional methods like X-ray diffraction (XRD) and Raman spectroscopy, as their accuracy is restricted to tens of MPa [88, 89]. Moreover, the performance, including frequency stability and coherence time, of these non-uniform stress-induced degeneracy-broken mechanical modes has not been systematically studied.

In this work, we analyzed the asymmetric stress along the x- and y-axes of the zinc-blende crystal structure SiC membrane by thoroughly examining the resonance characteristics of all 57 mechanical modes. By deriving the membrane resonance frequency under asymmetric stress and fitting the resonance characteristics, we found a strong agreement between theoretical predictions and experimental results. This approach allows us to obtain the exact biaxial stress distribution with a resolution well below MPa, surpassing the capabilities of current commercial membrane stress analysis instruments. Subsequently, we measured the frequency stability of the aforementioned degeneracy-broken mechanical modes. The results from the Allan variance measurements indicate that the dominant oscillator noise is primarily white noise, and no frequency drift was observed over the 40-day measurement period. This represents the highest level of frequency stability reported in the literature for micro- and nano-mechanical oscillators, outperforming even bulk silica glass. Benefiting from exceptionally high frequency stability and quality factors, we demonstrate highly efficient coherent state swapping between a pair of degenerate-broken mechanical modes in their ground state, achieving over 78% efficiency in a cavity electromechanical system composed of the mechanical resonator and a superconducting microwave circuit cavity.

## Results

### Stress-Anisotropy induced Non-Degenerated Mode-pairs

Considering a square membrane with unequal stress in x and y directions, as shown in Fig. 1a, the out-of-plane resonance characteristics of the membrane resonator can be derived from the Euler-Bernoulli equation:

$$\sigma_x \frac{\partial^2 w}{\partial^2 x} + \sigma_y \frac{\partial^2 w}{\partial^2 y} = \rho \frac{\partial^2 w}{\partial t^2} \quad (1)$$

Where the  $w$  represents the transverse displacement,  $\sigma_x(\sigma_y)$  is the corresponding stress in x(y) direction,  $\rho$  is the mass density. The resonance frequencies can be determined through the application of boundary conditions and are expressed as follows:

$$\frac{\omega_{mn}}{2\pi} = \frac{1}{2L} \sqrt{\frac{m^2 \sigma_x + n^2 \sigma_y}{\rho}} \quad (2)$$

Where the  $L$  is the side length of the square membrane,  $m(n)$  denotes the antinode numbers along the x(y) direction. In the scenario of isotropic stress ( $\sigma = \sigma_x = \sigma_y$ ) on the membrane, the resonance frequencies shorted as the general form  $\omega_{m,n}/2\pi = \sqrt{(m^2 + n^2)\sigma}/(4L^2\rho)$ . The detailed derivation of Eq. (2) is provided in Supplementary Note 1.

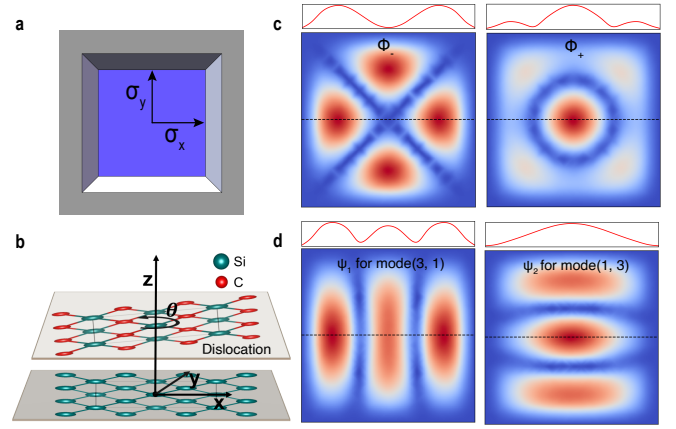


**Fig. 1 | Schematic of the SiC membrane resonator and out-of-plane mode-shapes with isotropic and anisotropic stress.**

**a** Schematic of the square SiC membrane resonator, where the grey color represents the silicon frame, and the blue region indicates the SiC membrane window. The quantities  $\sigma_x$  and  $\sigma_y$  denote the stresses along the x- and y-axis, respectively. **b** A simplified model demonstrating the origin of stress biaxial anisotropy, arising from the relative rotation dislocation between the substrate silicon lattice  $\langle 100 \rangle$  and the overlying silicon carbide lattice (3C phase) during the growth process. **c** Surface shapes of two out-of-plane modes, denoted as  $\Phi_-$  and  $\Phi_+$ , under isotropic stress applied to the square membrane. **d** Surface shapes of mode(3,1) and mode(1,3), with the mode indices determined by the number of antinodes along the x- and y-directions. The panel at the top of each mode shape presents the vibration amplitude (red-curves) across the center, as indicated by the dashed lines in the mode shape figures.

In our experiment, the SiC membrane is in 3C-phase and features a 2D square shape. Notably, it experiences unequal stresses along the x-axis and y-axis. Figure 1a illustrates a schematic of a standard suspended SiC membrane chip, depicting a square membrane subjected to differential stresses along the x- and y axes. The lattice plane dislocation between the 3C-SiC membrane and the substrate Si  $\langle 100 \rangle$  illustrates the origin of the anisotropic stress [90–93], as shown in Fig. 1b.

To illustrate the impact of stress anisotropy, figure 1c and 1d compare the vibrational mode shapes of a square membrane under isotropic and anisotropic stress, as determined by finite element simulations (FES). In the case of isotropic stress, using the second degenerate mode pair of a square membrane as an example, their vibration amplitude shapes (referred to as mode shapes) exhibit distinct characteristics, as shown in Fig. 1c. It demonstrates that the maximum amplitude appears off-center of the membrane for the  $\Phi_-$  and at the center for  $\Phi_+$ . These two vibration amplitudes  $\Phi_{\pm}$  can be further expressed as superpositions of another two orthogonal mode shapes with 90-degree rotational symmetry. Mathematically, we express this as  $\Phi_{\pm} = \alpha\phi_{(3,1)} \pm \beta\phi_{(1,3)}$ , where the mode shapes of  $\phi_{(3,1)}$  and  $\phi_{(1,3)}$  resemble those amplitudes of mode(3,1) and

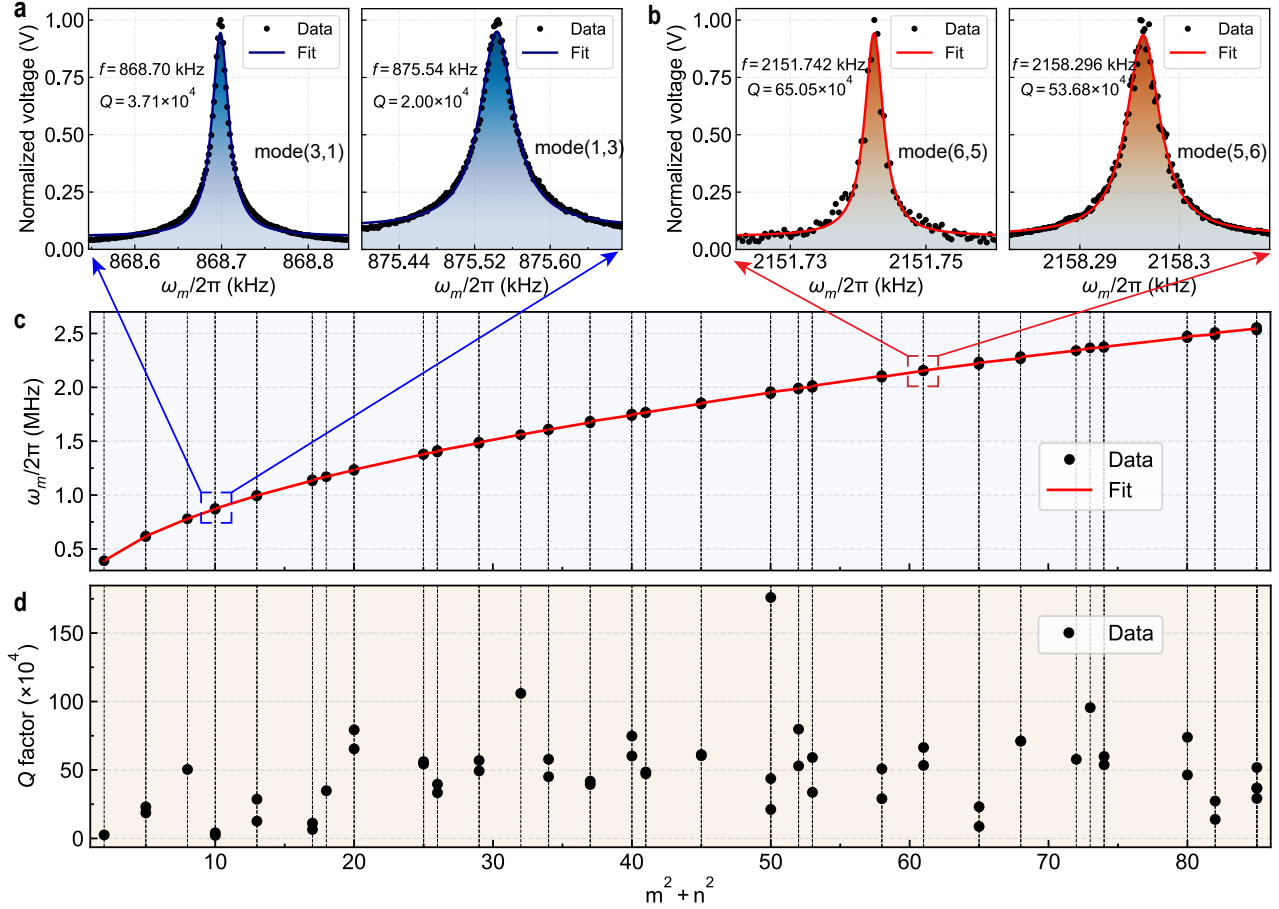


**Fig. 2** | Typical vibration spectra of degenerate modes induced by anisotropic stress at low frequencies **a** and high frequencies **b** in a square SiC membrane at room temperature. **c** Dependence of the experimental and theoretical resonance frequencies for 57 modes on the sum of the squares of corresponding mode indices  $m$  and  $n$ . Black circular dots represent the experimental results and the red line corresponds to the theoretical fit. The fitted results show the stress in x- and y axes are 242.95 MPa and 245.81 MPa, respectively, with the coefficient of determination ( $R^2$ ) exceeding 99.99%. **d** The quality factors of all 57 modes are measured at room temperature, from which mode breaking induced by the stress anisotropy is evident as the distinct quality factor values.

mode(1,3) in Fig. 1d. The indices, such as (1,3) or (3,1), represent the number of antinodes of the mode shape along the x- and y-axes, respectively. The  $\alpha$  and  $\beta$  represent the occupied proportions associated with each mode shape.

As shown in Fig. 1d, both mode(3,1) and mode(1,3) exhibit significant vibration amplitude in the center of the membrane. The surface amplitude for a cross-section through the center of the membrane (indicated by the black dashed line in the mode shape) is shown in the top panel of each figure. It reveals that only the  $\Phi_+$  mode behaviors a large amplitude at the membrane's center. Under anisotropic stress, however, two modes can exhibit similar mode shapes, related by a  $\pi/2$  rotation about the z-axis, as shown in Fig. 1d. Later in the text, these modes are designated as  $\psi_1$  for  $\phi_{(3,1)}$  [mode(3,1)] and  $\psi_2$  for  $\phi_{(1,3)}$  [mode(1,3)]. It is noted that both  $\psi_1$  and  $\psi_2$  exhibit significant amplitude at the center of the membrane, which is advantageous for constructing the multi-

mode cavity optomechanical system based on the single cavity mode [34, 72, 73, 94, 95].

### Anisotropic stress analysis of the 2D SiC-membrane

The mechanical vibration characteristics of breaking modes induced by stress anisotropy in the SiC membrane resonator at room temperature were investigated using a laser Doppler vibrometer. The SiC membrane has dimensions of  $500 \mu\text{m} \times 500 \mu\text{m} \times 50 \text{nm}$  with crystalline of 3C-phase, and its schematic is illustrated in Fig. 1a. The mechanical vibration of the resonator was excited by microwaves provided by a lock-in amplifier via a probe positioned above it. The resonant mechanical spectra of the out-of-plane modes were detected by the laser Doppler vibrometer and analyzed using the lock-in amplifier. All measurements were conducted in a vacuum chamber maintained at a pressure of  $1 \times 10^{-4}$  Pa.

Figure 2a shows a typical vibration spectrum of the breaking

modes in both low frequencies and high frequencies, resulting from the anisotropic stresses of the membrane along the  $x$ - and  $y$ -directions. The low-order modes with frequencies of 868.70 kHz and 875.54 kHz correspond to mode(3,1) and mode(1,3), and the high-order modes with frequencies of 2.152 MHz and 2.158 MHz correspond to mode(6,5) and mode(5,6), respectively, with the mode indices determined from FES (see Supplementary Note 2). The independent vibration nature of each mode is manifest due to the high  $Q$  factors.

The dependence of the resonance frequencies on the sum of squares of mode indices  $m$  and  $n$  is shown in Fig. 2c. The detailed information about each measured mechanical mode with indices  $(m, n)$  are displayed in the Supplementary Note 2. The choice of  $m^2 + n^2$  as variables for the fitting function Eq. (2) is based on the independent and iterative nature of the indices  $m$  and  $n$ , which describe the antinode numbers of the mode shape along different directions. Excellent agreement is observed between measured frequencies and theoretical predictions across the full 390 kHz-2.556 MHz range for all 57 modes. The fitted results reveal that the stress along the  $x$ -axis and  $y$ -axis are 242.95 MPa and 245.81 MPa, respectively. The discrimination of subtle discrepancies in stress through resonance characterization offers a simple and highly accurate method for evaluating internal anisotropic stress in materials.

The quality factors of all modes are demonstrated in Fig. 2d, which displays that the almost modes have the  $Q$  factors on the order of hundreds of thousands. This high  $Q$ -factor is attributed to the membrane's high aspect ratio and significant tensile stresses, both of which contribute to the reduction of mechanical energy through the dilution dissipation mechanism. The dilution factor  $D_Q$  of the square membrane resonator can be determined theoretically as follows [96]:

$$D_Q = \frac{1}{\lambda} \left[ 1 + \frac{\pi^2 \lambda (m^2 + n^2)}{4} \right]^{-1} \quad (3)$$

$$\lambda = \sqrt{\frac{4D}{\bar{\sigma} h L^2}} \quad (4)$$

$$D = \frac{E h^3}{12(1 - \nu^2)} \quad (5)$$

where  $h$  is the thickness of the membrane,  $E$  and  $\nu$  denote the Young's modulus and Poisson ratio of the device material, respectively. The dilution factor of the mode(3,1) is determined to be approximately 370 with the consideration of  $h = 50$  nm,  $L = 500$   $\mu$ m,  $\bar{\sigma} = 244.38$  MPa,  $E = 437$  GPa [97, 98], and  $\nu = 0.268$  [99].

In addition to reducing dissipation, high and anisotropic tensile stress will lead to degeneracy breaking, resulting in near-degenerate mode pairs with similar mode shapes and resonance frequencies. Next, we will demonstrate how these modes facilitate the development of multimode optomechanical/electromechanical systems, which consist of a single optical mode coupled to pairs of mechanical modes.

### Electromechanical interface for extremely stable and long-

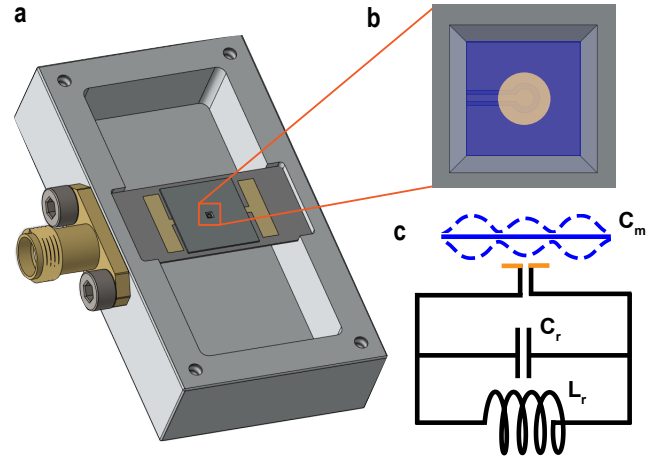


**Fig. 3** | **a** The schematic of the cavity electromechanical system, comprising a 3D aluminum rectangular cavity and a SiC membrane. Microwave signal pumping and readout are performed through the SMA port. **b** A zoom-in of the electromechanical chip. The SiC membrane is flip-chip mounted onto the bottom planar capacitor circuit. The gray, blue, and yellow regions correspond to the silicon frame, the SiC membrane, and the metal-coated area. **c** The lumped element mode of the cavity electromechanical system, sketched the mechanical mode(3,1) (blue) coupling to the capacity plate of LC circuits (orange). The electromechanical interaction is mediated by changes in mechanical capacitance  $C_m$  as the membrane vibrates.  $C_r$  and  $L_r$  represent the equivalent capacitance and inductance of the 3D metal cavity.

### lived mechanical mode pairs

In this section, we demonstrate the state swapping between extremely stable  $\psi_1$  and  $\psi_2$  based on a cavity electromechanical operations. The detailed schematic of the device is shown in Fig. 3a. The system primarily consists of a 3D aluminum rectangular cavity and a SiC membrane that has been metalized to enable electromechanical coupling based on a mechanical capacitor structure. The position-sensitive mechanical capacitor chip is mounted at the center of the 3D cavity, with a single port utilized for applying tones or reading out the system's transmission. Figure 3b shows the configuration of the mechanical capacitor, which is composed of the metalized SiC membrane and the bottom planar circuit capacitor. The electromechanical interaction is enabled by the changes in capacitance caused by the membrane's vibration, and the lumped element model of the electromechanical interaction is demonstrated in Fig. 3c. Similar device configurations and measurement techniques for this system have been discussed in our previous works [73, 81]. The mechanical performance of one mode pair  $\psi_1$  and  $\psi_2$  was first characterized at cryogenic temperatures and then followed by demonstrations of ground-state cooling and coherent-state swapping within this mode pair.

The cavity electromechanical device was located in the mixing chamber stage of a dilution refrigerator with a temperature of 10 mK. The characteristics of the SiC membrane resonator

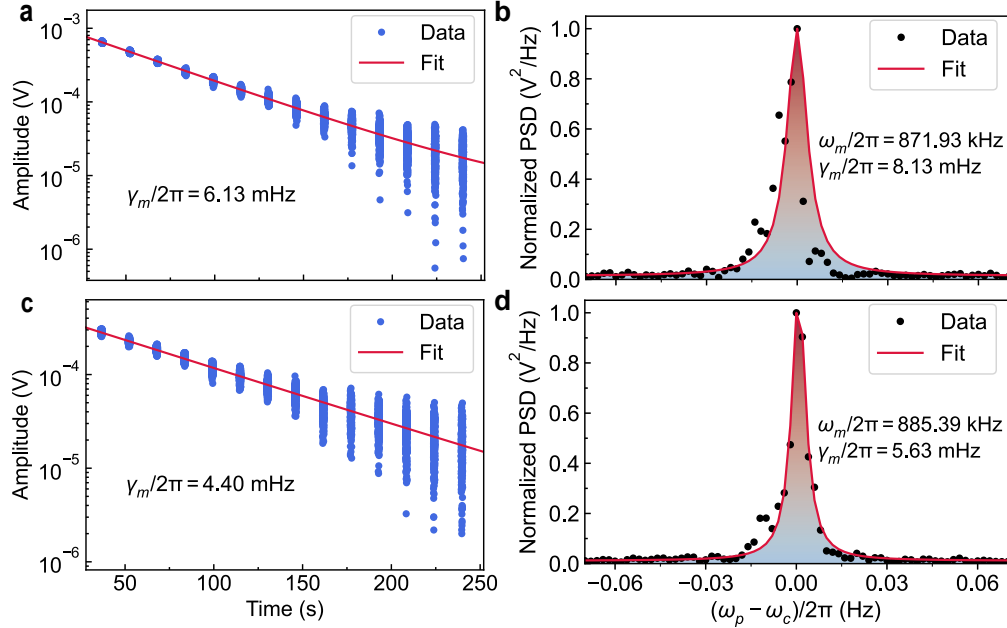


**Fig. 4 | Characterization of the mechanical properties of one mode pair at 10 mK using stroboscopic ring-down method and measuring the power spectrum density.** The time dependence of the vibration amplitude for **a** mechanical mode(3,1) and **c** mode(1,3) measured using the stroboscopic ring-down method. The power spectrum density (PSD) of **b** for the mechanical mode(3,1) and **d** for the mode(1,3). The  $Q$  factors of the SiC membrane resonator are determined by  $Q = \omega_m/\gamma_m$  with  $Q = 1.07 \times 10^8$  for mode(3,1) and  $Q = 1.57 \times 10^8$  for mode(1,3), respectively.

and cavity can be obtained by the spectrum analyzer and the vector network analyzer. It reveals that the microwave cavity has a resonance frequency of  $\omega_c/2\pi = 5.39$  GHz and a total linewidth of  $\kappa_{\text{tot}}/2\pi = 200.25$  kHz, with an external dissipation rate of  $\kappa_{\text{ext}}/2\pi = 100.25$  kHz and an intrinsic dissipation rate of  $\kappa_{\text{int}}/2\pi = 100$  kHz, respectively.

The characteristics of the SiC membrane resonator were determined using both the energy stroboscopic ring-down method and vibration spectrum analysis. In the stroboscopic ring-down method, the membrane resonator was first excited by a differential signal composed of tones at the red sideband frequency ( $\omega_r = \omega_c - \omega_m$ ) and the cavity frequency ( $\omega_c$ ), here  $\omega_m$  represents the resonance frequency of membrane resonator. Subsequently, the red sideband tones were turned off, and cavity-frequency tones were periodically turned on, in which two sidebands with frequencies at  $\omega_r = \omega_c - \omega_m$  and  $\omega_b = \omega_c + \omega_m$  will be generated. The free decay of mechanical vibration energy was detected using a spectrum analyzer, with the acquisition frequency set near the red sideband here.

The experimental results obtained from the stroboscopic ring-down method for  $\psi_1$  and  $\psi_2$  are presented in Fig. 4a and 4c, respectively. It demonstrates an exponential decay in the vibration amplitude of the SiC membrane resonator over time. The periodic disappearance of amplitude is attributed to the intermittent cessation of cavity-frequency tones. Compared with continuous measurement methods, the stroboscopic approach mitigates the influence of the microwave field on the membrane, thereby improving the accuracy of the measured energy

dissipation rate. Theoretical fitting reveals energy dissipation rates of 6.13 mHz and 4.4 mHz for  $\psi_1$  and  $\psi_2$ , respectively.

Additionally, direct detection of the mechanical vibration spectrum was employed to characterize the SiC membrane resonator, where the oscillation of the SiC membrane resonator was excited by environmental thermal fluctuations. By continuously applying the red sideband tone, the characteristics of the mechanical oscillator can be extracted from the up-conversion sideband spectrum with frequency at  $\omega_c$ . The vibration spectrum of the SiC membrane resonator for mode  $\psi_1$  and  $\psi_2$  are shown in Fig. 4b and 4d, respectively. The Lorentzian fitting reveals that the resonance frequencies and dissipation rates are 871.93 kHz and 8.13 mHz for the  $\psi_1$  and 885.39 kHz and 5.63 mHz for  $\psi_2$ , respectively. It illustrates that this device operates in the resolved-sideband regime ( $\kappa_c < \omega_m$ ). Correspondingly, the  $Q$  factors for the  $\psi_1$  and  $\psi_2$  are  $1.07 \times 10^8$  and  $1.57 \times 10^8$ , respectively.

The high  $Q$  factors observed at 10 mK are attributed to the exceptional thermal conductivity of silicon carbide, in addition to the dissipation dilution mechanism arising from stress and geometric nonlinearity. This behavior shows that thermoelastic dissipation of 3C-phase SiC decreases with temperature, even at 10 mK, a characteristic unattainable by most semiconductors and amorphous materials. The higher dissipation rate observed here, compared to the results from the stroboscopic method, is due to the fact that it represents the total dissipation rate of the mechanical oscillator, which includes both the thermal decoherence rate and the dephasing rate [100], rather

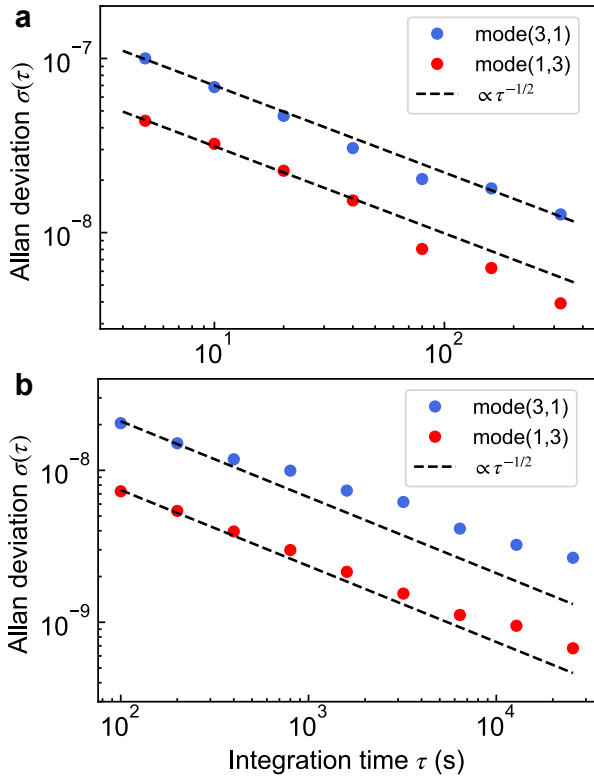


**Fig. 5** | Allan deviation  $\sigma(\tau)$  versus integration time  $\tau$  for modes(3,1) and mode(1,3). Measurements were performed using **a** 5s and **b** 100s sampling intervals. Black dashed lines are the least-squares fits to the  $\sigma(\tau) = A\tau^{-1/2}$  noise model, where  $A$  is the fitting parameter.

than only the thermal decoherence rate measured by the stroboscopic ring-down method. Therefore, a pure dephasing rate as low as 1.23 mHz can be extracted for this SiC membrane resonator.

### Superior frequency stability at cryogenic temperatures

The SiC resonator exhibits superior frequency stability owing to its low thermal expansion coefficient, vibration-mode-insensitive volumetric deformation, and the high thermal conductivity that suppresses thermoelastic dissipation by rapidly relaxing thermal gradient-induced stresses. The frequency stability of the resonator can be analyzed by Allan deviation, which can be described mathematically as [101, 102]:

$$\sigma(\tau) = \sqrt{\frac{1}{2(N-1)} \sum_{i=1}^{N-1} \left( \frac{\bar{f}_{i+1} - \bar{f}_i}{f_0} \right)^2} \quad (6)$$

Where  $N$  is the total number of sampled resonance frequencies ( $\bar{f}_1, \bar{f}_2, \dots, \bar{f}_N$ ), each averaged over an integration time interval  $\tau$ .  $f_0$  is the reference resonance frequency of the resonator.

The integration time dependence of the Allan deviation for the degeneracy-broken pair of mode(3,1) and mode(1,3) is presented in Fig. 5, with distinct sampling intervals of 5s (Fig. 5

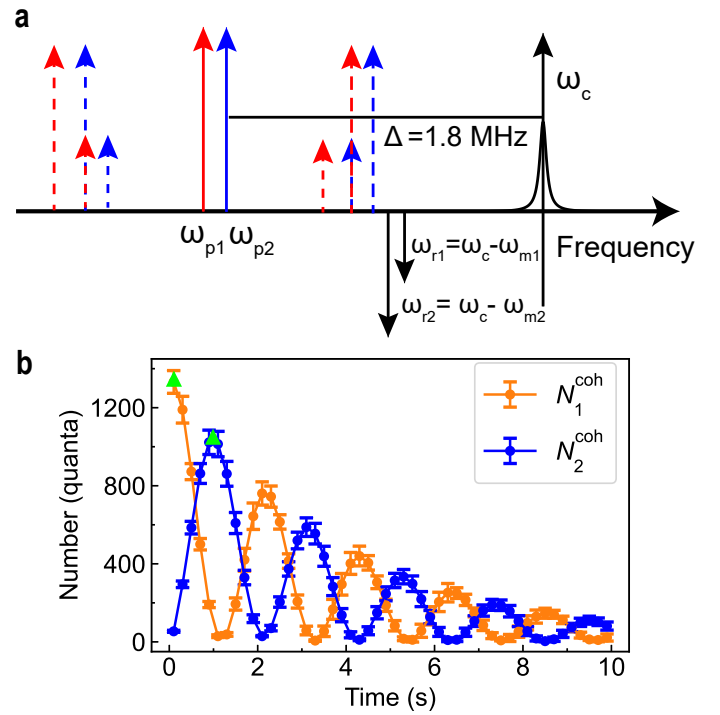


**Fig. 6** | **a** The frequencies in the optomechanical STIRAP scheme. The black downward arrows indicate the red sidebands, whose separations from the cavity resonance frequency match the frequencies of the two mechanical modes. The swapping tones are represented by the solid red and blue upward arrows, while the corresponding sidebands are shown as dashed arrows. The swapping between the two mechanical modes is induced due to the overlapping of the sidebands. **b** Dependence of the coherent occupancies of two mechanical modes on swapping time.

a) and 100s (Fig. 5 b). These intervals were chosen to characterize noise origins and analyze long-term frequency stability. The minimum sampling time was constrained by both the high  $Q$  factors of the resonator and the spectral acquisition methodology. The experimental data (colored circles) are well fitted by the characteristic power-law relationship  $A\tau^{-1/2}$ , indicative of white frequency noise.

Figure 5 shows the Allan deviation decreases monotonically across all integration times, regardless of whether they are shorter or longer than the resonator's response time  $\tau_r = 1/(\pi\gamma_m)$ , and the best  $\sigma(\tau) = 6 \times 10^{-10}$  are obtained at  $\tau = 3 \times 10^4$ s. The observed  $\tau^{-1/2}$  scaling in all integration time identifies white frequency-modulation noise as the dominant noise source, which we attribute primarily to detection noise [103]. As summarized in Table I, the measured frequency stability of our degeneracy-broken mode pair demonstrates superior performance compared with previously reported resonators fabricated from alternative materials.

### Coherent state swapping within the mode pair

Benefiting from an extremely small dephasing rate and su-

**Table I** | Comparison of frequency stability of resonator fabricated from different materials.

Material	Structure	Mode	$f$ (MHz)	$Q$ ( $\times 10^3$ )	Freq. stability (ppm)	Duration	T (K)	Best $\sigma(\tau)$	Ref.
Si	Center-anchored	Flexural	0.15	33	$\pm 5$	2500 hours	Room	$8 \times 10^{-6}$ ( $\tau \approx 10^5$ s)	[104]
Si	Clamped-clamped	Flexural	0.21	20	$\pm 9$	6000 s	323	$3 \times 10^{-7}$ ( $\tau \approx 10$ s)	[105]
Si	Clamped-clamped	Flexural	0.068	-	$\pm 87.7$	600 s	Room	$1.2 \times 10^{-8}$ ( $\tau \approx 11$ s)	[106]
Si	Cantilever	Flexural	0.589	8	0.4	60 s	Room	$5 \times 10^{-9}$ ( $\tau \approx 100$ ms)	[107]
Si nanowire	Clamped-clamped	Flexural	187.9	-	0.15	1 s	25	$6 \times 10^{-8}$ ( $\tau \approx 8$ s)	[108]
Silica glass	Twin-microbottle	Breathing	56.7	3.5	-	-	Room	$1 \times 10^{-10}$ ( $\tau \approx 30$ ms)	[109]
Si/SiO <sub>2</sub>	Center-anchored	Extensional	6.759	41	-3.6	40 hours	20	$2.7 \times 10^{-9}$ ( $\tau \approx 1$ s)	[110]
Carbon nanotube	Clamped-clamped	Flexural	1865	-	3	30 s	5.5	$2 \times 10^{-6}$ ( $\tau \approx 30$ s)	[111]
Carbon nanotube	Clamped-clamped	Flexural	28.9	-	$\pm 52$	60 s	4.2	$3 \times 10^{-5}$ ( $\tau \approx 30$ s)	[112]
Carbon nanotube	Clamped-clamped	Flexural	55.6	480	$\pm 4.5$	500 s	0.03	$4 \times 10^{-7}$ ( $\tau \approx 100$ s)	[113]
AlN/Si	Clamped-clamped	Flexural	65	4230	-	-	Room	$4 \times 10^{-9}$ ( $\tau \approx 1$ s)	[114]
AlN/Si <sub>3</sub> N <sub>4</sub>	Cantilever	Flexural	0.088	0.098	-	-	Room	$2 \times 10^{-8}$ ( $\tau \approx 10$ s)	[115]
Mo/Si	Center-anchored	Lamé	18.284	309.9	-	-	Room	$5 \times 10^{-9}$ ( $\tau \approx 100$ ms)	[116]
Si <sub>3</sub> N <sub>4</sub>	Membrane	Flexural	0.09	1180	-	-	Room	$4 \times 10^{-9}$ ( $\tau \approx 0.1$ s)	[117]
Si <sub>3</sub> N <sub>4</sub>	Membrane	Flexural	0.076	2533	$\pm 2.6$	300 s	Room	$9 \times 10^{-9}$ ( $\tau \approx 0.2$ s)	[118]
Si <sub>3</sub> N <sub>4</sub>	Membranes	Flexural	0.188	30	-	-	Room	$3 \times 10^{-7}$ ( $\tau \approx 1$ s)	[119]
Si <sub>3</sub> N <sub>4</sub>	Membranes	Flexural	0.082	97	-	-	Room	$8 \times 10^{-7}$ ( $\tau \approx 1$ s)	[120]
Si <sub>3</sub> N <sub>4</sub>	Clamped-clamped	Flexural	2.844	378.7	0.7	10 s	Room	$2 \times 10^{-8}$ ( $\tau \approx 1$ s)	[121]
SiN string	Clamped-clamped	Flexural	0.264	300	-	-	Room	$7 \times 10^{-8}$ ( $\tau \approx 20$ s)	[122]
SiC	Clamped-clamped	Flexural	428.2	2.5	2	500 s	22K	-	[123]
SiC	Membrane	Flexural	0.885	$1.57 \times 10^5$	$\pm 0.02$	214 hours	0.01	$6 \times 10^{-10}$ ( $\tau \approx 3 \times 10^4$ s)	Our work

perior frequency stability, these mode pairs are promising candidates for constructing long-lived phononic memories. The stimulated Raman adiabatic passage (STIRAP) in optomechanics exhibits significant potential for transferring states with high fidelity, attributed to the intermediary dark state involved in this process. Here, we employ the optomechanical STIRAP scheme to carry out the state swapping between mode(3,1) and mode(1,3) by modulating inter-mode coupling at their difference frequency.

The pumping tones and the corresponding generated sidebands of our STIRAP scheme are illustrated in Fig. 6a. The downward-pointing black arrows labeled  $\omega_{r1}$  ( $\omega_{r2}$ ) indicate the red sideband frequencies of modes  $\psi_1$  and  $\psi_2$ . The shifts relative to the cavity resonance frequency  $\omega_c$  match the resonance frequencies of modes  $\psi_1$  and  $\psi_2$ , respectively, which demonstrates the resolved sideband condition. The solid red (blue) upward-pointing arrows denote the pumping tones at frequencies  $\omega_{p1}$  ( $\omega_{p2}$ ), while the dashed arrows in corresponding colors represent their associated sidebands. One pumping tone applied to two mechanical modes will generate four sidebands, resulting in a total of eight sidebands with two pumping tones. To mitigate the effects of cavity damping and unmatched motional sidebands, we set the pumping tones with a larger detuning from the cavity resonance at  $\Delta/2\pi = 1.8$  MHz. The separation between the pumping tones matches the frequency

difference of the two mechanical modes [124]. The swapping of the states between  $\psi_1$  and  $\psi_2$  occurs as a result of the overlap of the sidebands, as illustrated in Fig. 6a.

The complete state-swapping process involves four primary phases: cooling, excitation, swapping, and readout. Initially, two mechanical modes are cooled to near their quantum ground states using their individual red sideband tones simultaneously. Next, one mode, here is the  $\psi_1$ , is excited by the difference frequency signal through concurrent injection of tones at frequencies of cavity  $\omega_c$  and red sideband  $\omega_c - \omega_{m1}$ . After turning off the excitation tones, the swapping tones are injected to facilitate the swapping processes. Once the swapping tones are turned off, the mechanical state is read out via blue sideband amplification. Further details regarding the characterization in cooling and readout can be found in our previous works [73, 81].

By repeating the aforementioned four processes and varying the swapping time in each experiment, we can characterize the swapping dynamics. The dependence of coherent phonons occupation of two mechanical modes on swapping time is shown in Fig. 6b, illustrating that mechanical excitations oscillate between the two modes as the swapping time increases, with maximum occupancies alternately exchanging. The swapping period is 2.1 seconds. As the swapping time increases, the coherent occupancies of the mechanical modes decrease and

eventually reach thermal equilibrium. The transfer efficiency is 78.18%, defined as the ratio of the number of phonons in  $\psi_2$  at the end of the first swapping to the number of phonons in  $\psi_1$  at the beginning of the swapping [124], as indicated by the green triangles.

## Discussion

Asymmetric stress induced degeneracy-broken offers a pathway to develop multimode opto-/electro-mechanical systems utilizing multiple phononic mode pairs within a single mechanical oscillator. By performing collective fitting on a measured set of 57 mechanical modes, we uncover deviations in biaxial nonuniform stress on the order of MPa, supports a remarkably high resolution for stress analysis in thin films. In contrast, detecting stress anisotropy necessitates additional adjustments, such as geometric configurations [125, 126], polarization tuning of light [115, 127], and signal enhancement techniques [128, 129]. Our method, which combines dynamic resonance measurements with theoretical analysis, provides a simpler detection process and more accurate stress values for characterizing stress asymmetry in thin films.

The results from the Allan deviation measurements highlight the exceptional frequency stability of the degenerate-broken mechanical mode pairs. The dominant oscillator noise is primarily white noise, and importantly, no frequency drift was observed over the 40-day measurement period. This level of frequency stability represents the highest reported in the literature for micro- and nano-mechanical oscillators, even surpassing that of bulk silica glass. By integrating a superconducting resonant cavity with the SiC membrane-based electromechanical chip to form a cavity electromechanical system, we experimentally demonstrated high-fidelity state exchange between a degeneracy-breaking mode pair. The experimental results show that the transfer efficiency exceeds 78%, which is attributed to the high quality factors of the mechanical modes and the strong coupling between the two mechanical modes and the shared cavity mode. These findings hold significant potential for advancing quantum information storage, scalable quantum computing, distributed quantum networks, and quantum simulation research based on multiple phonon modes via stress engineering [10, 64, 130, 131].

## Method

### Device fabrication

The device measured at room temperature utilizes a commercial 3C-phase silicon carbide (Norcada PSCX5050A). The SiC membrane features a window with the dimensions of  $500\ \mu\text{m} \times 500\ \mu\text{m}$  and a thickness of 50 nm, supported by a  $400\ \mu\text{m}$  thick silicon frame.

At cryogenic temperature, the cavity electromechanical device is composed of a 3D aluminum (Al) superconducting cavity and a mechanical capacitor chip. The 3D Al rectangular cavity is precision-machined and polished to ensure low microwave absorption and scattering. The mechanical capacitor

chip consists of two parallel plates: the upper plate is the metallized SiC membrane and the bottom plate is a planar metal circuit capacitor. The metallization of the SiC membrane is achieved through the deposition of Al via electron beam evaporation (JEB-4, Adnanotek). The bottom planar capacitor features an H-shaped electrode and a concentric niobium (Nb) arc and circle as its center. The planar capacitor electrode is fabricated from a 120 nm thick niobium (Nb) film, deposited on a high-resistivity silicon substrate using physical vapor deposition (Syskey Technology, SP-IC4-A06). The pattern is defined by laser direct-writing using DWL 66+ laser lithography tool (Heidelberg Instruments), and the unwanted Nb film is removed via reactive ion etching (RIE-10NR, Samco inc.). A commercial ACC $\mu$ RA flip-chip bonder is employed to align the center of the upper plate with the center of the bottom capacitor electrode.

### Measurement methods

The mechanical spectrum was employed to characterize the properties of the SiC membrane resonator. At room temperature, the mechanical modes were excited by microwaves via a probe positioned above it, and the resonant mechanical spectrum is acquired by a laser Doppler vibrometer (ONOSOKKI LV-1800) and analyzed by a lock-in amplifier (Zurich Instruments UHFLI, 600 MHz). All measurements were conducted in a vacuum chamber maintained at a pressure of  $1 \times 10^{-4}$  Pa. The resonant frequencies and quality factors were extracted by fitting the mechanical spectrum to the Lorentzian function.

At cryogenic temperatures, the cavity electromechanical device was detected at the 10 mK stage of a dilution refrigerator (BlueFors LD400). The detection was performed via reflection measurements using a circulator. In order to avoid the saturation of high electron mobility transistor (HEMT), a canceling tone and the output tone were integrated through a directional coupler, the reflected pump tone can be destructive interference by fine-tuning the amplitude and phase of the cancelling tone. An arbitrary waveform generator (Tektronix AWG5014C) was combined with a mixer to generate pulse tones, including sideband pump tone ( $\omega_c - \omega_{m1,m2}$ ,  $\omega_{p1}$ ,  $\omega_{p2}$ ), amplified tone ( $\omega_c + \omega_{m1,m2}$ ), and signal tone ( $\omega_c$ ). These tones were combined using a broadband power splitter at room temperature and transmitted to the device through low-loss coaxial lines. High-isolation microwave switches were positioned after each mixer to ensure precise on-off control of individual tones, with the switch control signals and mixer trigger signals generated simultaneously via the marker channel and analog channel of the AWG, respectively. The real-time signal was acquired using a spectrum analyzer (Tektronix RSA5126B). For S21 parameter measurements of the device, the PNA (Rohde & Schwarz ZNB20) probe tone was integrated into the input line. All instruments were phase-locked to a 10 MHz rubidium frequency standard.

**Data availability** The data that support the findings of this study are available from the corresponding authors upon reasonable request.

- [1] C. Herring, Role of low-energy phonons in thermal conduction, *Phys. Rev.* **95**, 954 (1954).
- [2] S. K. Sinha, Phonons in semiconductors, *Critical Reviews in Solid State and Material Sciences* **3**, 273 (1973).
- [3] R. Hillenbrand, T. Taubner, and F. Keilmann, Phonon-enhanced light-matter interaction at the nanometre scale, *Nature* **418**, 159 (2002).
- [4] D. Garg, A. K. Chauhan, and A. Biswas, Adiabatic transfer of energy fluctuations between membranes inside an optical cavity, *Phys. Rev. A* **96**, 023837 (2017).
- [5] L. Fan, K. Y. Fong, M. Poot, and H. X. Tang, Cascaded optical transparency in multimode-cavity optomechanical systems, *Nature Communications* **6**, 5850 (2015).
- [6] K. Stannigel, P. Komar, S. J. M. Habraken, S. D. Bennett, M. D. Lukin, P. Zoller, and P. Rabl, Optomechanical quantum information processing with photons and phonons, *Phys. Rev. Lett.* **109**, 013603 (2012).
- [7] D. P. Lake, M. Mitchell, D. D. Sukachev, and P. E. Barclay, Processing light with an optically tunable mechanical memory, *Nature Communications* **12**, 663 (2021).
- [8] M. J. A. Schuetz, E. M. Kessler, G. Giedke, L. M. K. Vandersypen, M. D. Lukin, and J. I. Cirac, Universal quantum transducers based on surface acoustic waves, *Phys. Rev. X* **5**, 031031 (2015).
- [9] L. Tian and H. Wang, Optical wavelength conversion of quantum states with optomechanics, *Phys. Rev. A* **82**, 053806 (2010).
- [10] S. J. M. Habraken, K. Stannigel, M. D. Lukin, P. Zoller, and P. Rabl, Continuous mode cooling and phonon routers for phononic quantum networks, *New Journal of Physics* **14**, 115004 (2012).
- [11] B. Vermersch, P.-O. Guimond, H. Pichler, and P. Zoller, Quantum state transfer via noisy photonic and phononic waveguides, *Phys. Rev. Lett.* **118**, 133601 (2017).
- [12] J. M. Dobrindt and T. J. Kippenberg, Theoretical analysis of mechanical displacement measurement using a multiple cavity mode transducer, *Phys. Rev. Lett.* **104**, 033901 (2010).
- [13] R. Burgwal and E. Verhagen, Enhanced nonlinear optomechanics in a coupled-mode photonic crystal device, *Nature Communications* **14**, 1526 (2023).
- [14] R. Riedinger, A. Wallucks, I. Marinković, C. Löschnauer, M. Aspelmeyer, S. Hong, and S. Gröblacher, Remote quantum entanglement between two micromechanical oscillators, *Nature* **556**, 473 (2018).
- [15] C. F. Ockeloen-Korppi, E. Damskägg, J.-M. Pirkkalainen, M. Asjad, A. A. Clerk, F. Massel, M. J. Woolley, and M. A. Sillanpää, Stabilized entanglement of massive mechanical oscillators, *Nature* **556**, 478 (2018).
- [16] T.-X. Lu, B. Li, Y. Wang, D.-Y. Wang, X. Xiao, and H. Jing, Directional quantum-squeezing-enabled nonreciprocal enhancement of entanglement, *Phys. Rev. Appl.* **22**, 064001 (2024).
- [17] J. Ghosh, S. Mondal, S. K. Varshney, and K. Debnath, Simultaneous control of quantum phase synchronization and entanglement dynamics in a gain-loss optomechanical cavity system, *Phys. Rev. A* **109**, 023512 (2024).
- [18] J. Huang, D.-G. Lai, and J.-Q. Liao, Thermal-noise-resistant optomechanical entanglement via general dark-mode control, *Phys. Rev. A* **106**, 063506 (2022).
- [19] U. Kemiktarak, M. Durand, M. Metcalfe, and J. Lawall, Mode competition and anomalous cooling in a multimode phonon laser, *Phys. Rev. Lett.* **113**, 030802 (2014).
- [20] J. Sheng, X. Wei, C. Yang, and H. Wu, Self-organized synchronization of phonon lasers, *Phys. Rev. Lett.* **124**, 053604 (2020).
- [21] L. Mercadé, K. Pelka, R. Burgwal, A. Xuereb, A. Martínez, and E. Verhagen, Floquet phonon lasing in multimode optomechanical systems, *Phys. Rev. Lett.* **127**, 073601 (2021).
- [22] L. Mercier de Lépinay, C. F. Ockeloen-Korppi, D. Malz, and M. A. Sillanpää, Nonreciprocal transport based on cavity Floquet modes in optomechanics, *Phys. Rev. Lett.* **125**, 023603 (2020).
- [23] N. R. Bernier, L. D. Tóth, A. Koottandavida, M. A. Ioannou, D. Malz, A. Nunnenkamp, A. K. Feofanov, and T. J. Kippenberg, Nonreciprocal reconfigurable microwave optomechanical circuit, *Nature Communications* **8**, 604 (2017).
- [24] A. Seif, W. DeGottardi, K. Esfarjani, and M. Hafezi, Thermal management and non-reciprocal control of phonon flow via optomechanics, *Nature Communications* **9**, 1207 (2018).
- [25] K. Fang, J. Luo, A. Metelmann, M. H. Matheny, F. Marquardt, A. A. Clerk, and O. Painter, Generalized non-reciprocity in an optomechanical circuit via synthetic magnetism and reservoir engineering, *Nature Physics* **13**, 465 (2017).
- [26] J. P. Mathew, J. d. Pino, and E. Verhagen, Synthetic gauge fields for phonon transport in a nano-optomechanical system, *Nature Nanotechnology* **15**, 198 (2020).
- [27] F. Ruesink, M.-A. Miri, A. Alù, and E. Verhagen, Nonreciprocity and magnetic-free isolation based on optomechanical interactions, *Nature Communications* **7**, 13662 (2016).
- [28] H. Xu, L. Jiang, A. A. Clerk, and J. G. E. Harris, Nonreciprocal control and cooling of phonon modes in an optomechanical system, *Nature* **568**, 65 (2019).
- [29] W. H. P. Nielsen, Y. Tsaturyan, C. B. Møller, E. S. Polzik, and A. Schliesser, Multimode optomechanical system in the quantum regime, *Proceedings of the National Academy of Sciences* **114**, 62 (2017).
- [30] P. Piergentili, L. Catalini, M. Bawaj, S. Zippilli, N. Malossi, R. Natali, D. Vitali, and G. D. Giuseppe, Two-membrane cavity optomechanics, *New Journal of Physics* **20**, 083024 (2018).
- [31] M. Chegnizadeh, M. Scigliuzzo, A. Youssefi, S. Kono, E. Guzovskii, and T. J. Kippenberg, Quantum collective motion of macroscopic mechanical oscillators, *Science* **386**, 1383 (2024).
- [32] M. J. Weaver, F. Buters, F. Luna, H. Eerkens, K. Heeck, S. de Man, and D. Bouwmeester, Coherent optomechanical state transfer between disparate mechanical resonators, *Nature Communications* **8**, 824 (2017).
- [33] P. Piergentili, W. Li, R. Natali, N. Malossi, D. Vitali, and G. D. Giuseppe, Two-membrane cavity optomechanics: non-linear dynamics, *New Journal of Physics* **23**, 073013 (2021).
- [34] S. Wu, Y. Liu, Q. Liu, S.-P. Wang, Z. Chen, and T. Li, Hybridized frequency combs in multimode cavity electromechanical system, *Phys. Rev. Lett.* **128**, 153901 (2022).
- [35] A. B. Shkarin, N. E. Flowers-Jacobs, S. W. Hoch, A. D. Kashkanova, C. Deutsch, J. Reichel, and J. G. E. Harris, Optically mediated hybridization between two mechanical modes, *Phys. Rev. Lett.* **112**, 013602 (2014).
- [36] K. Schneider, Y. Baumgartner, S. Hönl, P. Welter, H. Hahn, D. J. Wilson, L. Czornomaz, and P. Seidler, Optomechanics with one-dimensional gallium phosphide photonic crystal cavities, *Optica* **6**, 577 (2019).
- [37] M. Asano, G. Zhang, T. Tawara, H. Yamaguchi, and H. Okamoto, Near-field cavity optomechanical coupling in a

- compound semiconductor nanowire, *Communications Physics* **3**, 230 (2020).
- [38] F. Fogliano, B. Besga, A. Reigue, P. Heringlake, L. Mercier de Lépinay, C. Vaneph, J. Reichel, B. Pigeau, and O. Arcizet, Mapping the cavity optomechanical interaction with subwavelength-sized ultrasensitive nanomechanical force sensors, *Phys. Rev. X* **11**, 021009 (2021).
- [39] C. Doolin, P. H. Kim, B. D. Hauer, A. J. R. MacDonald, and J. P. Davis, Multidimensional optomechanical cantilevers for high-frequency force sensing, *New Journal of Physics* **16**, 035001 (2014).
- [40] K. Srinivasan, H. Miao, M. T. Rakher, M. Davanço, and V. Aksyuk, Optomechanical transduction of an integrated silicon cantilever probe using a microdisk resonator, *Nano Letters* **11**, 791 (2011).
- [41] Y. Huang, J. G. F. Flores, Z. Cai, M. Yu, D.-L. Kwong, G. Wen, L. Churchill, and C. W. Wong, A low-frequency chip-scale optomechanical oscillator with 58 kHz mechanical stiffening and more than 100th-order stable harmonics, *Scientific Reports* **7**, 4383 (2017).
- [42] A. G. Primo, P. V. Pinho, R. Benevides, S. Gröblacher, G. S. Wiederhecker, and T. P. M. Alegre, Dissipative optomechanics in high-frequency nanomechanical resonators, *Nature Communications* **14**, 5793 (2023).
- [43] G. S. MacCabe, H. Ren, J. Luo, J. D. Cohen, H. Zhou, A. Sipahigil, M. Mirhosseini, and O. Painter, Nano-acoustic resonator with ultralong phonon lifetime, *Science* **370**, 840 (2020).
- [44] A. Zivari, R. Stockill, N. Fiaschi, and S. Gröblacher, Non-classical mechanical states guided in a phononic waveguide, *Nature Physics* **18**, 789 (2022).
- [45] J. Bochmann, A. Vainsencher, D. D. Awschalom, and A. N. Cleland, Nanomechanical coupling between microwave and optical photons, *Nature Physics* **9**, 712 (2013).
- [46] J. M. Fink, M. Kalaei, A. Pitanti, R. Norte, L. Heinzle, M. Davanço, K. Srinivasan, and O. Painter, Quantum electromechanics on silicon nitride nanomembranes, *Nature Communications* **7**, 12396 (2016).
- [47] J. M. Pate, M. Goryachev, R. Y. Chiao, J. E. Sharping, and M. E. Tobar, Casimir spring and dilution in macroscopic cavity optomechanics, *Nature Physics* **16**, 1117 (2020).
- [48] W. Yang, S. A. Gerke, K. W. Ng, Y. Rao, C. Chase, and C. J. Chang-Hasnain, Laser optomechanics, *Scientific Reports* **5**, 13700 (2015).
- [49] M. Eichenfield, J. Chan, R. M. Camacho, K. J. Vahala, and O. Painter, Optomechanical crystals, *Nature* **462**, 78 (2009).
- [50] U. Kemiktarak, M. Durand, M. Metcalfe, and J. Lawall, Mode competition and anomalous cooling in a multimode phonon laser, *Phys. Rev. Lett.* **113**, 030802 (2014).
- [51] Y. Seis, T. Capelle, E. Langman, S. Saarinen, E. Planz, and A. Schliesser, Ground state cooling of an ultracoherent electromechanical system, *Nature Communications* **13**, 1507 (2022).
- [52] J. Guo, J. Chang, X. Yao, and S. Gröblacher, Active-feedback quantum control of an integrated low-frequency mechanical resonator, *Nature Communications* **14**, 4721 (2023).
- [53] C. Meng, G. A. Brawley, S. Khademi, E. M. Bridge, J. S. Bennett, and W. P. Bowen, Measurement-based preparation of multimode mechanical states, *Science Advances* **8**, eabm7585 (2022).
- [54] S. Sbarra, L. Waquier, S. Suffit, A. Lemaître, and I. Favero, Multimode optomechanical weighting of a single nanoparticle, *Nano Letters* **22**, 710 (2022).
- [55] I.-T. Chen, B. Li, S. Lee, S. Chakravarthi, K.-M. Fu, and M. Li, Optomechanical ring resonator for efficient microwave-optical frequency conversion, *Nature Communications* **14**, 7594 (2023).
- [56] Y. Yu, X. Xi, and X. Sun, Observation of mechanical bound states in the continuum in an optomechanical microresonator, *Light: Science & Applications* **11**, 328 (2022).
- [57] F. Tebbenjohanns, M. L. Mattana, M. Rossi, M. Frimmer, and L. Novotny, Quantum control of a nanoparticle optically levitated in cryogenic free space, *Nature* **595**, 378 (2021).
- [58] J. Piotrowski, D. Windey, J. Vijayan, C. Gonzalez-Balletero, A. de los Ríos Sommer, N. Meyer, R. Quidant, O. Romero-Isart, R. Reimann, and L. Novotny, Simultaneous ground-state cooling of two mechanical modes of a levitated nanoparticle, *Nature Physics* **19**, 1009 (2023).
- [59] M. Zhao and K. Fang, Mechanical bound states in the continuum for macroscopic optomechanics, *Opt. Express* **27**, 10138 (2019).
- [60] H. Tong, S. Liu, M. Zhao, and K. Fang, Observation of phonon trapping in the continuum with topological charges, *Nature Communications* **11**, 5216 (2020).
- [61] P. Kharel, G. I. Harris, E. A. Kittlaus, W. H. Renninger, N. T. Otterstrom, J. G. E. Harris, and P. T. Rakich, High-frequency cavity optomechanics using bulk acoustic phonons, *Science Advances* **5**, eaav0582 (2019).
- [62] P. Kharel, Y. Chu, D. Mason, E. A. Kittlaus, N. T. Otterstrom, S. Gertler, and P. T. Rakich, Multimode strong coupling in cavity optomechanics, *Phys. Rev. Appl.* **18**, 024054 (2022).
- [63] A. S. Kuznetsov, K. Biermann, A. A. Reynoso, A. Fainstein, and P. V. Santos, Microcavity phononitons – a coherent optical-to-microwave interface, *Nature Communications* **14**, 5470 (2023).
- [64] U. von Lüpke, I. C. Rodrigues, Y. Yang, M. Fadel, and Y. Chu, Engineering multimode interactions in circuit quantum acoustodynamics, *Nature Physics* **20**, 564 (2024).
- [65] H. Li, S. A. Tadesse, Q. Liu, and M. Li, Nanophotonic cavity optomechanics with propagating acoustic waves at frequencies up to 12 GHz, *Optica* **2**, 826 (2015).
- [66] R. W. Andrews, R. W. Peterson, T. P. Purdy, K. Cicak, R. W. Simmonds, C. A. Regal, and K. W. Lehnert, Bidirectional and efficient conversion between microwave and optical light, *Nature Physics* **10**, 321 (2014).
- [67] D. J. Wilson, C. A. Regal, S. B. Papp, and H. J. Kimble, Cavity optomechanics with stoichiometric SiN films, *Phys. Rev. Lett.* **103**, 207204 (2009).
- [68] T. Bağcı, A. Simonsen, S. Schmid, L. G. Villanueva, E. Zeuthen, J. Appel, J. M. Taylor, A. Sørensen, K. Usami, A. Schliesser, and E. S. Polzik, Optical detection of radio waves through a nanomechanical transducer, *Nature* **507**, 81 (2014).
- [69] A. P. Higginbotham, P. S. Burns, M. D. Urmey, R. W. Peterson, N. S. Kampel, B. M. Brubaker, G. Smith, K. W. Lehnert, and C. A. Regal, Harnessing electro-optic correlations in an efficient mechanical converter, *Nature Physics* **14**, 1038 (2018).
- [70] R. D. Delaney, M. D. Urmey, S. Mittal, B. M. Brubaker, J. M. Kindem, P. S. Burns, C. A. Regal, and K. W. Lehnert, Superconducting-qubit readout via low-backaction electro-optic transduction, *Nature* **606**, 489 (2022).
- [71] S. S. Rao, Vibration of membranes, in *Vibration of Continuous Systems* (John Wiley & Sons, Ltd, 2006) Chap. 13, pp. 420–456.
- [72] A. Noguchi, R. Yamazaki, M. Ataka, H. Fujita, Y. Tabuchi, T. Ishikawa, K. Usami, and Y. Nakamura, Ground state cooling of a quantum electromechanical system with a silicon nitride membrane in a 3D loop-gap cavity, *New Journal of Physics* **18**, 103036 (2016).

- [73] Y. Liu, Q. Liu, H. Sun, M. Chen, S. Wang, and T. Li, Coherent memory for microwave photons based on long-lived mechanical excitations, *npj Quantum Information* **9**, 80 (2023).
- [74] Y. Liu, Q. Liu, S. Wang, Z. Chen, M. A. Sillanpää, and T. Li, Optomechanical anti-lasing with infinite group delay at a phase singularity, *Phys. Rev. Lett.* **127**, 273603 (2021).
- [75] D.-G. Lai, J.-F. Huang, X.-L. Yin, B.-P. Hou, W. Li, D. Vitali, F. Nori, and J.-Q. Liao, Nonreciprocal ground-state cooling of multiple mechanical resonators, *Phys. Rev. A* **102**, 011502 (2020).
- [76] J. Huang, D.-G. Lai, C. Liu, J.-F. Huang, F. Nori, and J.-Q. Liao, Multimode optomechanical cooling via general dark-mode control, *Phys. Rev. A* **106**, 013526 (2022).
- [77] J. Huang, D.-G. Lai, and J.-Q. Liao, Controllable generation of mechanical quadrature squeezing via dark-mode engineering in cavity optomechanics, *Phys. Rev. A* **108**, 013516 (2023).
- [78] J. Huang, D.-G. Lai, and J.-Q. Liao, Thermal-noise-resistant optomechanical entanglement via general dark-mode control, *Phys. Rev. A* **106**, 063506 (2022).
- [79] D.-G. Lai, J.-Q. Liao, A. Miranowicz, and F. Nori, Noise-tolerant optomechanical entanglement via synthetic magnetism, *Phys. Rev. Lett.* **129**, 063602 (2022).
- [80] J. Huang, C. Liu, X.-W. Xu, and J.-Q. Liao, Dark-mode theorems for quantum networks, arXiv preprint arXiv:2312.06274 [10.48550/arXiv.2312.06274](https://arxiv.org/abs/2312.06274) (2023).
- [81] Y. Liu, H. Sun, Q. Liu, H. Wu, M. A. Sillanpää, and T. Li, Degeneracy-breaking and long-lived multimode microwave electromechanical systems enabled by cubic silicon-carbide membrane crystals, *Nature Communications* **16**, 1207 (2025).
- [82] D. Hoch, K.-J. Haas, L. Moller, T. Sommer, P. Soubelet, J. J. Finley, and M. Poot, Efficient optomechanical mode-shape mapping of micromechanical devices, *Micromachines* **12**, [10.3390/mi12080880](https://doi.org/10.3390/mi12080880) (2021).
- [83] A. Sanz-Jiménez, J. J. Ruz, E. Gil-Santos, O. Malvar, S. García-López, P. M. Kosaka, Á. Cano, M. Calleja, and J. Tamayo, Square membrane resonators supporting degenerate modes of vibration for high-throughput mass spectrometry of single bacterial cells, *ACS Sensors* **8**, 2060 (2023).
- [84] C.-H. Liu, I. S. Kim, and L. J. Lauhon, Optical control of mechanical mode-coupling within a MoS<sub>2</sub> resonator in the strong-coupling regime, *Nano Letters* **15**, 6727 (2015).
- [85] A. B. Shkarin, N. E. Flowers-Jacobs, S. W. Hoch, A. D. Kashkanova, C. Deutsch, J. Reichel, and J. G. E. Harris, Optically mediated hybridization between two mechanical modes, *Phys. Rev. Lett.* **112**, 013602 (2014).
- [86] S. Chakram, Y. S. Patil, L. Chang, and M. Vengalattore, Dissipation in ultrahigh quality factor SiN membrane resonators, *Phys. Rev. Lett.* **112**, 127201 (2014).
- [87] A. Barg, Y. Tsaturyan, E. Belhage, W. H. P. Nielsen, C. B. Møller, and A. Schliesser, Measuring and imaging nanomechanical motion with laser light, *Applied Physics B* **123**, 8 (2016).
- [88] R. S. Jakubek and M. D. Fries, Calibration of Raman wavenumber in large Raman images using a mercury-argon lamp, *Journal of Raman Spectroscopy* **51**, 1172 (2020).
- [89] S. O. F. Kagi, High precision in Raman frequency achieved using real-time calibration with a neon emission line: Application to three-dimensional stress mapping observations, *Applied Spectroscopy* **62**, 1084 (2008).
- [90] C. Long, S. A. Ustin, and W. Ho, Structural defects in 3C-SiC grown on Si by supersonic jet epitaxy, *Journal of Applied Physics* **86**, 2509 (1999).
- [91] F. Ernst and P. Pirouz, The formation mechanism of planar defects in compound semiconductors grown epitaxially on {100} silicon substrates, *Journal of Materials Research* **4**, 834 (1989).
- [92] F. La Via, A. Severino, R. Anzalone, C. Bongiorno, G. Litrico, M. Mauceri, M. Schoeler, P. Schuh, and P. Wellmann, From thin film to bulk 3C-SiC growth: Understanding the mechanism of defects reduction, *Materials Science in Semiconductor Processing* **78**, 57 (2018).
- [93] M. Zimbone, M. Mauceri, G. Litrico, E. G. Barbagiovanni, C. Bongiorno, and F. La Via, Protrusions reduction in 3C-SiC thin film on Si, *Journal of Crystal Growth* **498**, 248 (2018).
- [94] S. Gigan, H. R. Böhm, M. Paternostro, F. Blaser, G. Langer, J. B. Hertzberg, K. C. Schwab, D. Bäuerle, M. Aspelmeyer, and A. Zeilinger, Self-cooling of a micromirror by radiation pressure, *Nature* **444**, 67 (2006).
- [95] X. Ren, J. Pan, M. Yan, J. Sheng, C. Yang, Q. Zhang, H. Ma, Z. Wen, K. Huang, H. Wu, and H. Zeng, Dual-comb optomechanical spectroscopy, *Nature Communications* **14**, 5037 (2023).
- [96] Y. Liu, J. P. Zhen, W. X. Yang, X. D. Zheng, S. L. Guo, Y. Zhang, P. Yang, K. H. Lv, J. Qiu, and G. J. Liu, Research on dissipation dilution mechanism and boundary dissipation suppression technique for high-stress graphene nanoelectromechanical resonator, *Journal of Physics: Conference Series* **2557**, 012064 (2023).
- [97] T. Matsumoto, T. Nose, Y. Nagata, K. Kawashima, T. Yamada, H. Nakano, and S. Nagai, Measurement of high-temperature elastic properties of ceramics using a laser ultrasonic method, *Journal of the American Ceramic Society* **84**, 1521 (2001).
- [98] D. Varshney, S. Shriya, M. Varshney, N. Singh, and R. Khenata, Elastic and thermodynamical properties of cubic (3C) silicon carbide under high pressure and high temperature, *Journal of Theoretical and Applied Physics* **9**, 221 (2015).
- [99] F. H. Stillinger and T. A. Weber, Computer simulation of local order in condensed phases of silicon, *Phys. Rev. B* **31**, 5262 (1985).
- [100] A. Youssefi, S. Kono, M. Chegnizadeh, and T. J. Kippenberg, A squeezed mechanical oscillator with millisecond quantum decoherence, *Nature Physics* **19**, 1697 (2023).
- [101] D. W. Allan, Statistics of atomic frequency standards, *Proceedings of the IEEE* **54**, 221 (1966).
- [102] P. Sadeghi, A. Demir, L. G. Villanueva, H. Kähler, and S. Schmid, Frequency fluctuations in nanomechanical silicon nitride string resonators, *Phys. Rev. B* **102**, 214106 (2020).
- [103] P. Sadeghi, A. Demir, L. G. Villanueva, H. Kähler, and S. Schmid, Frequency fluctuations in nanomechanical silicon nitride string resonators, *Phys. Rev. B* **102**, 214106 (2020).
- [104] B. Kim, R. Candler, M. Hopcroft, M. Agarwal, W.-T. Park, and T. Kenny, Frequency stability of wafer-scale encapsulated mems resonators, in *The 13th International Conference on Solid-State Sensors, Actuators and Microsystems, 2005. Digest of Technical Papers. TRANSDUCERS '05.*, Vol. 2 (2005) pp. 1965–1968 Vol. 2.
- [105] M. Pandit, A. Mustafazade, G. Sobreviela, C. Zhao, X. Zou, and A. A. Seshia, Experimental observation of temperature and pressure induced frequency fluctuations in silicon mems resonators, *Journal of Microelectromechanical Systems* **30**, 500 (2021).
- [106] D. Antonio, D. H. Zanette, and D. López, Frequency stabilization in nonlinear micromechanical oscillators, *Nature Communications* **3**, 806 (2012).
- [107] S. Olcum, N. Cermak, S. C. Wasserman, K. S. Christine, H. Atsumi, K. R. Payer, W. Shen, J. Lee, A. M. Belcher, S. N. Bhatia, and S. R. Manalis, Weighing nanoparticles in solution at the attogram scale, *Proceedings of the National Academy of Sciences* **111**, 1310 (2014).

- [108] X. Feng, R. He, P. Yang, and M. Roukes, Phase noise and frequency stability of very-high frequency silicon nanowire nanomechanical resonators, in *TRANSDUCERS 2007 - 2007 International Solid-State Sensors, Actuators and Microsystems Conference* (2007) pp. 327–330.
- [109] M. Asano, H. Yamaguchi, and H. Okamoto, Cavity optomechanical liquid level meter using a twin-microbottle resonator, arXiv preprint arXiv:2401.12529 [10.48550/arXiv.2401.12529](https://arxiv.org/abs/10.48550/arXiv.2401.12529) (2024).
- [110] C. A. Watkins, J. Lee, J. P. McCandless, H. J. Hall, and X.-L. F. Philip, Single-crystal silicon thermal-piezoresistive resonators as high-stability frequency references, *Journal of Microelectromechanical Systems* **34**, 15 (2025).
- [111] J. Chaste, A. Eichler, J. Moser, G. Ceballos, R. Rurali, and A. Bachtold, A nanomechanical mass sensor with yoctogram resolution, *Nature Nanotechnology* **7**, 301 (2012).
- [112] J. Schwender, I. Tsioutsios, A. Tavernarakis, Q. Dong, Y. Jin, U. Stauffer, and A. Bachtold, Improving the read-out of the resonance frequency of nanotube mechanical resonators, *Applied Physics Letters* **113**, 063104 (2018).
- [113] J. Moser, A. Eichler, J. Güttinger, M. I. Dykman, and A. Bachtold, Nanotube mechanical resonators with quality factors of up to 5 million, *Nature Nanotechnology* **9**, 1007 (2014).
- [114] T. Kaiser, S. M. E. H. Yousuf, J. Lee, A. Qamar, M. Rais-Zadeh, S. Mandal, and P. X.-L. Feng, Five low-noise stable oscillators referenced to the same multimode AlN/Si mems resonator, *IEEE Transactions on Ultrasonics, Ferroelectrics, and Frequency Control* **70**, 1213 (2023).
- [115] C. Song, L. Du, L. Qi, Y. Li, X. Li, and Y. Li, Residual stress measurement in a metal microdevice by micro Raman spectroscopy, *Journal of Micromechanics and Microengineering* **27**, 105014 (2017).
- [116] Y. Xiao, J. Han, K. Zhu, and G. Wu, A piezoelectric mechanically coupled lamé mode resonator with ultra-high Q, *Applied Physics Letters* **122**, 114101 (2023).
- [117] C. Zhang and R. St-Gelais, Demonstration of frequency stability limited by thermal fluctuation noise in silicon nitride nanomechanical resonators, *Applied Physics Letters* **122**, 193501 (2023).
- [118] N. Snell, C. Zhang, G. Mu, A. Bouchard, and R. St-Gelais, Heat transport in silicon nitride drum resonators and its influence on thermal fluctuation-induced frequency noise, *Phys. Rev. Appl.* **17**, 044019 (2022).
- [119] T. Manzanique, M. K. Ghatkesar, F. Alijani, M. Xu, R. A. Norte, and P. G. Steeneken, Resolution limits of resonant sensors, *Phys. Rev. Appl.* **19**, 054074 (2023).
- [120] H. Bešić, A. Demir, J. Steurer, N. Luhmann, and S. Schmid, Schemes for tracking resonance frequency for micro- and nanomechanical resonators, *Phys. Rev. Appl.* **20**, 024023 (2023).
- [121] E. Gavartin, P. Verlot, and T. J. Kippenberg, Stabilization of a linear nanomechanical oscillator to its thermodynamic limit, *Nature Communications* **4**, 2860 (2013).
- [122] P. Sadeghi, A. Demir, L. G. Villanueva, H. Kähler, and S. Schmid, Frequency fluctuations in nanomechanical silicon nitride string resonators, *Phys. Rev. B* **102**, 214106 (2020).
- [123] X. L. Feng, C. J. White, A. Hajimiri, and M. L. Roukes, A self-sustaining ultrahigh-frequency nanoelectromechanical oscillator, *Nature Nanotechnology* **3**, 342 (2008).
- [124] V. Fedoseev, F. Luna, I. Hedgepeth, W. Löffler, and D. Bouwmeester, Stimulated Raman adiabatic passage in optomechanics, *Phys. Rev. Lett.* **126**, 113601 (2021).
- [125] M. Ferrari and L. Lutterotti, Method for the simultaneous determination of anisotropic residual stresses and texture by x-ray diffraction, *Journal of Applied Physics* **76**, 7246 (1994).
- [126] N. Rossini, M. Dassisti, K. Benyounis, and A. Olabi, Methods of measuring residual stresses in components, *Materials & Design* **35**, 572 (2012).
- [127] T. Gries, L. Vandenbulcke, P. Simon, and A. Canizares, Anisotropic biaxial stresses in diamond films by polarized Raman spectroscopy of cubic polycrystals, *Journal of Applied Physics* **104**, 023524 (2008).
- [128] K. Kneipp, Surface-enhanced Raman scattering, *Physics Today* **60**, 40 (2007).
- [129] J. Langer, D. Jimenez de Aberasturi, J. Aizpurua, R. A. Alvarez-Puebla, B. Auguie, J. J. Baumberg, G. C. Bazan, S. E. J. Bell, A. Boisen, A. G. Brolo, J. Choo, D. Cialla-May, V. Deckert, L. Fabris, K. Faulds, F. J. Garcia de Abajo, R. Goodacre, D. Graham, A. J. Haes, C. L. Haynes, C. Huck, T. Itoh, M. Käll, J. Kneipp, N. A. Kotov, H. Kuang, E. C. Le Ru, H. K. Lee, J.-F. Li, X. Y. Ling, S. A. Maier, T. Mayerhöfer, M. Moskovits, K. Murakoshi, J.-M. Nam, S. Nie, Y. Ozaki, I. Pastoriza-Santos, J. Perez-Juste, J. Popp, A. Pucci, S. Reich, B. Ren, G. C. Schatz, T. Shegai, S. Schlücker, L.-L. Tay, K. G. Thomas, Z.-Q. Tian, R. P. Van Duyne, T. Vo-Dinh, Y. Wang, K. A. Willets, C. Xu, H. Xu, Y. Xu, Y. S. Yamamoto, B. Zhao, and L. M. Liz-Marzán, Present and future of surface-enhanced Raman scattering, *ACS Nano* **14**, 28 (2020).
- [130] M. C. Kuzyk and H. Wang, Scaling phononic quantum networks of solid-state spins with closed mechanical subsystems, *Phys. Rev. X* **8**, 041027 (2018).
- [131] Y. Chu, P. Kharel, T. Yoon, L. Frunzio, P. T. Rakich, and R. J. Schoelkopf, Creation and control of multi-phonon fock states in a bulk acoustic-wave resonator, *Nature* **563**, 666 (2018).

### Acknowledgements

We acknowledge the support of Beijing Natural Science Foundation (Z240007), National Natural Science Foundation of China (No. 92365210, No. 12374325, No. 12304387 and No. 62074091), Young Elite Scientists Sponsorship Program by CAST (Grant No. 2023QNRC001), and Beijing Municipal Science and Technology Commission (Grant No. Z221100002722011).

### Author contributions

H. S., Y. C., and Q. L. performed the room temperature Doppler laser measurements as well as low-temperature radio-frequency measurements. H. W. and Y. W. joined in the device fabrication. H. S., Y. C., Q. L., T. L., and Y. L. analyzed the measurement results and wrote the manuscript. All authors gave their final approval for publication.

### Competing interests

The authors declare no competing interests.

### Additional information

**Supplemental information** The online version contains supplemental material available at <http://...>